A Sliding-Mode Triboelectric Nanogenerator with Chemical Group Grated Structure by Shadow Mask Reactive Ion Etching

Wanyu Shang,[†,‡,#] Guang Qin Gu,[‡,§,∥,#] Feng Yang,[†] Lei Zhao,[†] Gang Cheng,*[,†] Zu-liang Du,*[,†] and Zhong Lin Wang*[,‡,§,⊥]

[†]Key Lab for Special Functional Materials, Ministry of Education, Henan University, Kaifeng 475004, China
[‡]Beijing Institute of Nanoenergy and Nanosystems, Chinese Academy of Sciences, Beijing 100083, China
[§]CAS Center for Excellence in Nanoscience, National Center for Nanoscience and Technology (NCNST), Beijing, 100190, China
[∥]University of Chinese Academy of Sciences, Beijing 100049, China
[⊥]School of Materials Science and Engineering, Georgia Institute of Technology, Atlanta, Georgia 30332-0245, United States

ABSTRACT: The sliding-mode triboelectric nanogenerator (S-TENG) with grated structure has important applications in energy harvest and active sensors; however its concavo-convex structure leads to large frictional resistance and abrasion. Here, we developed a S-TENG with a chemical group grated structure (S-TENG-CGG), in which the triboelectric layer's triboelectric potential has a positive−negative alternating charged structure. The triboelectric layer of the S-TENG-CGG was fabricated through a reactive ion etching process with a metal shadow mask with grated structure. In the etched region, the nylon film, originally positively charged as in friction with stainless steel, gained opposite triboelectric potential and became negatively charged because of the change of surface functional groups. The output signals of the S-TENG-CGG are alternating and the frequency is determined by both the segment numbers and the moving speed. The applications of the S-TENG-CGG in the charging capacitor and driving calculator are demonstrated. In the S-TENG-CGG, since there is no concavo-convex structure, the frictional resistance and abrasion are largely reduced, which enhances its performances in better stability and longer working time.

KEYWORDS: triboelectric nanogenerator, sliding mode, chemical group grated structure, reactive ion etching, nylon film
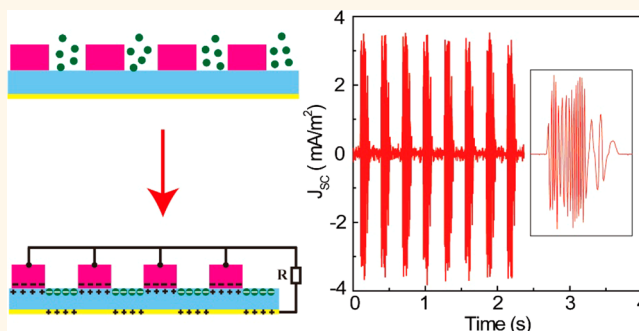
A shortage of energy and environmental issues are two major problems of human survival and development that have impelled extensive research in renewable energies. The triboelectric nanogenerator (TENG), based on the conjunction of contact electrification and an electrostatic induction effect,[1−3] has drawn much attention recently. TENG is a clean and sustainable power provider that can harvest energies often ignored by us from the environment such as human walking energy,[4−9] wind flowing energy,[10−12] water/ocean wave energy,[13−17] and so forth. TENGs have significant advantages of high efficiency, low cost, reliable robustness, and being environmental friendly.[18,19] TENGs have four working modes: vertical contact-separation mode,[20] lateral sliding mode,[21] single electrode mode[22] and freestanding tribo-electric-layer mode.[23]

Among the four modes, the lateral sliding mode is a promising mode to harvest energies from the relative sliding between objects and has clear analytical formulas.[24] It has been reported that a sliding mode triboelectric nanogenerator (S-

TENG) that combines with a grated structure can harvest ($2N − 1$) times the energy of tribo-charges for N segments device in one cycle.[25] Hence, S-TENGs with a grated structure have advantages in harvesting energy. Also, S-TENGs with a grated structure are usually used for sensors, such as motion sensors, speed sensors, acceleration sensors, and so forth.[26−29] However, there are drawbacks for S-TENGs with a grated structure. For example, since there are many segments in the triboelectric layer, the concavo-convex structure leads to large frictional resistance and abrasion, hence the grated structure is easily torn or worn out.

To mitigate the drawbacks, we herein report a S-TENG with a chemical group grated structure (S-TENG-CGG) that is based on a nylon triboelectric layer with positive−negative

 A
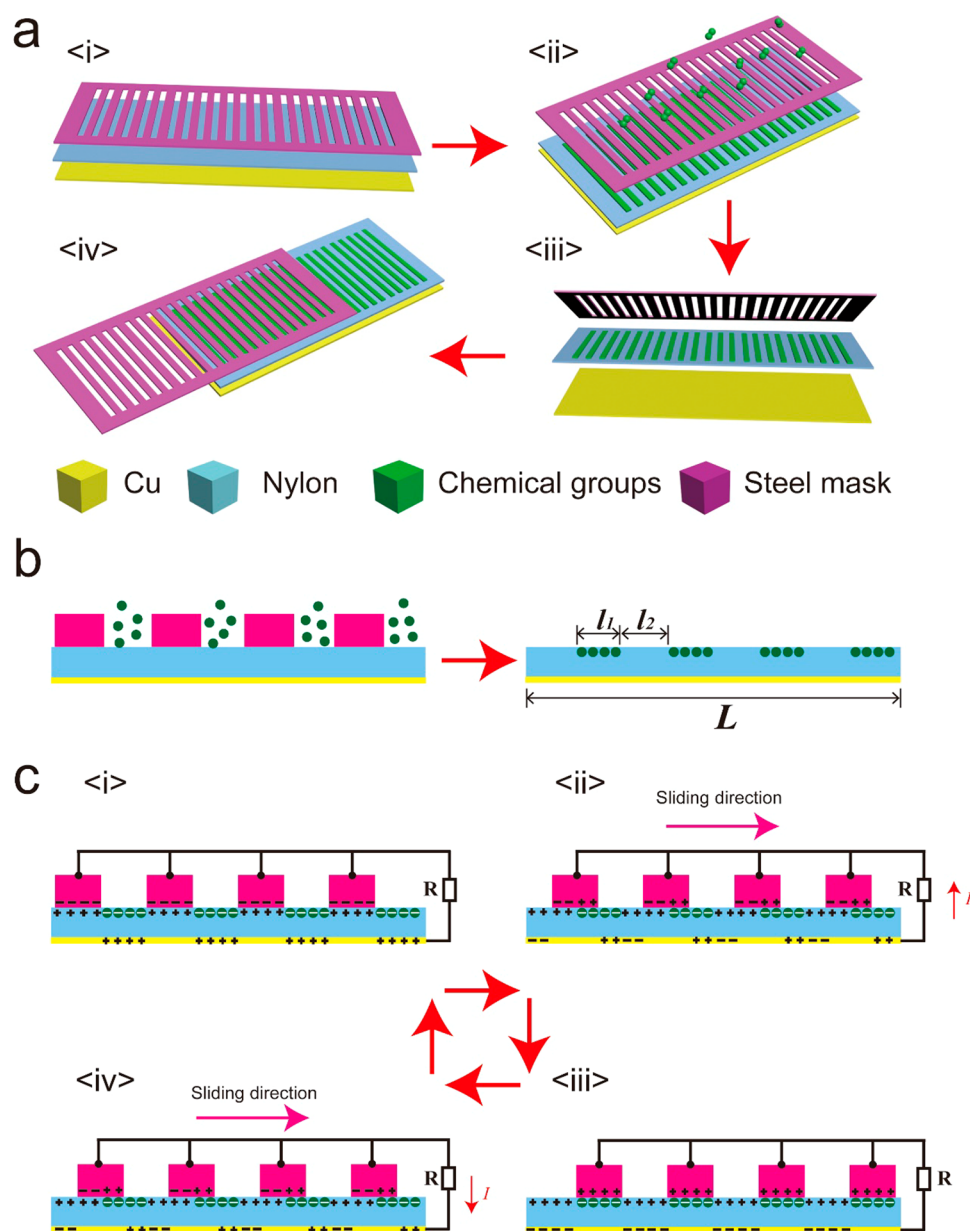
Figure 1. (a) Schematic image of the reactive ion etching processes (i−ii) and the fabrication processes of the S-TENG-CGG (iii−iv). (b) Cross section view of the reactive ion etching process and the as-prepared nylon film. (c) Diagram of working mechanism of the S-TENG-CGG.

alternating triboelectric potential, which was fabricated by a reactive ion etching (RIE) process by using a stainless steel shadow mask with grated structure. After the RIE process, the nylon film, originally positively charged as in friction with stainless steel, gained an opposite triboelectric potential with the grated structure and became negatively charged because of the change of surface functional groups. The output signals of the S-TENG-CGG are alternating and the frequency is determined by both the segment numbers and the moving speed. In the S-TENG-CGG, there is no concavo-convex structure and the frictional resistance and abrasion are smaller, which makes the S-TENG-CGG gain a longer working life.

RESULTS AND DISCUSSION

Schematics of the fabrication process of the S-TENG-CGG by an RIE process are shown in Figure 1. The S-TENG-CGG

device mainly consists of two groups of components: a nylon triboelectric layer with chemical group grated structure and a metal electrode with grated structure. To enable an alternating triboelectric potential during sliding, polyamide (nylon) and stainless steel were chosen as the materials for the triboelectric layer and metal electrode. Generally, nylon is positively charged when in friction with a stainless steel electrode, according to the triboelectric series;[30] however, it can change to be negatively charged when in friction with a stainless steel electrode after RIE treatment, which will be discussed below. In the fabrication of the triboelectric layer part, commercial nylon film was cleaned and a layer of copper (Cu) was deposited on it through magnetron sputtering. Then the film was cut and put under the stainless steel mask with a grated structure, as shown in Figure 1a. At last, the RIE process was made in a RIE machine, as shown in Figure 1a,ii. More details can be found in the
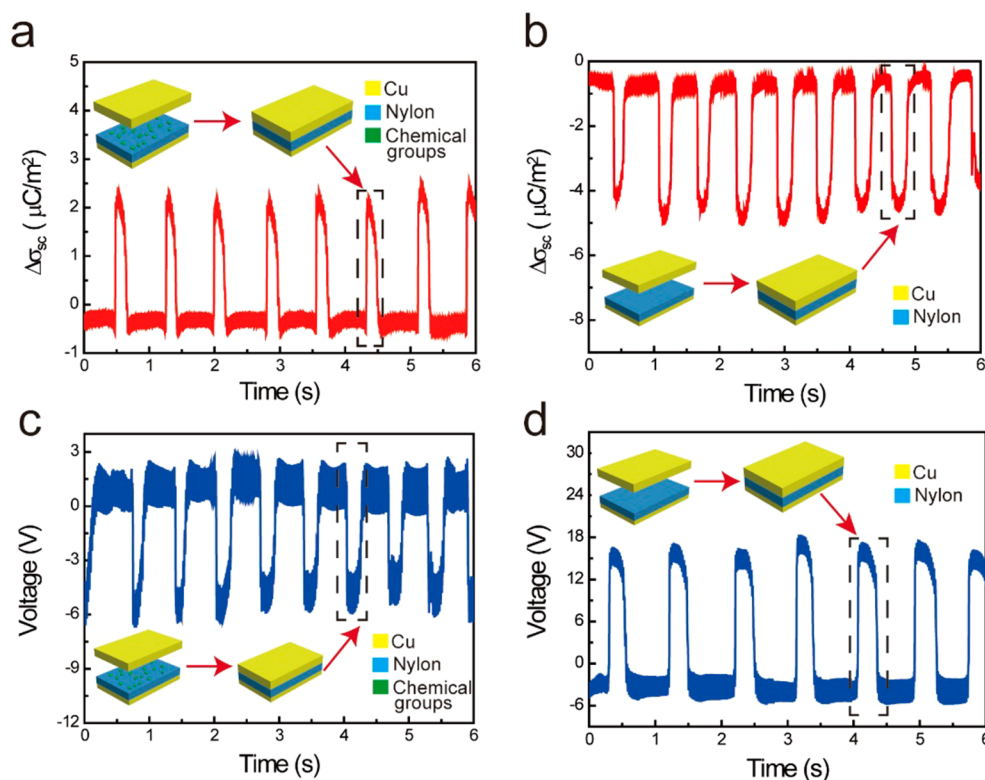
Figure 2. Transferred charge ($\Delta\sigma_{SC}$) of the RIE etched (a) and nonetched (b) TENG working in contact-separation mode. The open circuit voltage of the RIE etched (c) and nonetched (d) TENG working in contact-separation mode.

Experimental Section. After the RIE etching process, the as-prepared nylon films were used to assemble the S-TENGs. As for the metal electrode part, a new stainless steel mask with the same grated structure was used as both the triboelectric layer and the electrode. The width of the fingers and the gap between two adjacent fingers of the mask are the same, and three sizes of 700, 500, and 300 μm are used in our experiments, respectively. For the S-TENGs with different gap and finger width, we maintained the total effective length and width of the triboelectric layer with the same value, 2.5 and 2 cm, respectively, which ensures that these devices have the same total effective area (5 cm^2). Thus, the smaller width of each grated unit brings a larger segment number.

Cross-section schematic image of the RIE process is shown in Figure 1b. As discussed in detail in our group's previous report, the RIE process will lead to the fluorination reactions on the surface of nylon film, which changes its triboelectric potential.[31] Because of plasma discharging, CF_4 gas is decomposed into free radicals such as $\cdot CF_3$ and $:CF_2$ as illustrated by the following reaction equations.

$$CF_4 \rightarrow \cdot CF_3 + F\cdot \quad (1)$$

$$\cdot CF_3 \rightarrow : CF_2 + F\cdot \quad (2)$$

The unstable free radicals ($\cdot CF_3$ and $:CF_2$) tend to recombine into stable CF_4 gas. However, the presence of oxygen in the discharged region can effectively prevent such recombination,[32] producing more $\cdot F$ free radicals, as shown by the reaction equations below.

$$:CF_2 + O_2 \rightarrow \cdot CFO + F\cdot + O: \quad (3)$$

$$\cdot COF + : O \rightarrow CO_2 + F\cdot \quad (4)$$
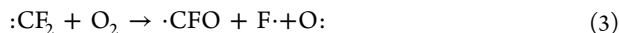
The existence of free radicals enables chemical reaction with nylon macromolecules. There are two possible reaction routes. The first is "implantation," in which free radicals containing fluorine enable substitution or addition. They can replace hydrogen or add to pi bonds of the aromatic rings to form reactive saturated intermediates.[33−35] The second is grafting, in which $:CF_2$ radials form successive chains.[35,36] Hence, in the etched zone by RIE the surface chemical groups and triboelectric potential are changed.

The operation principle of the S-TENG-CGG can be explained as the in-plane-sliding induced charge transfer, as shown in Figure 1c. After several cycles of sliding motion of stainless steel electrode, the triboelectric charges are generated in the nylon layer and reach equilibrium, where the regions in the nylon layer with and without RIE etching are negatively and positively charged, respectively. For demonstrating the current flow induced by the electrode motion, we set the position shown in Figure 1c,I as the initial stage, in which the positively-charged region in the nylon layer without etching is fully overlapping with the fingers of the steel electrode. In this case, the positive and negative tribo-charges in the nylon film are screened by the negative charges in the steel electrode and positive charges in the bottom Cu electrode, respectively. When the steel mask starts to slide rightward, the mask gradually moves from the overlapping position of original nylon to the RIE etched zone, (Figure 1c,ii). In this case, for reaching new electrical equilibrium, some positive charges in the Cu electrode flow into the steel electrode, and some negative charges in the steel electrode flow into the Cu electrode, which produces a transient current in the external load. Once the steel mask electrode reaches the fully overlapping position with the RIE etched zone (Figure 1c,iii), all of the positive charges in the Cu electrode are transferred into the steel electrode, all of the
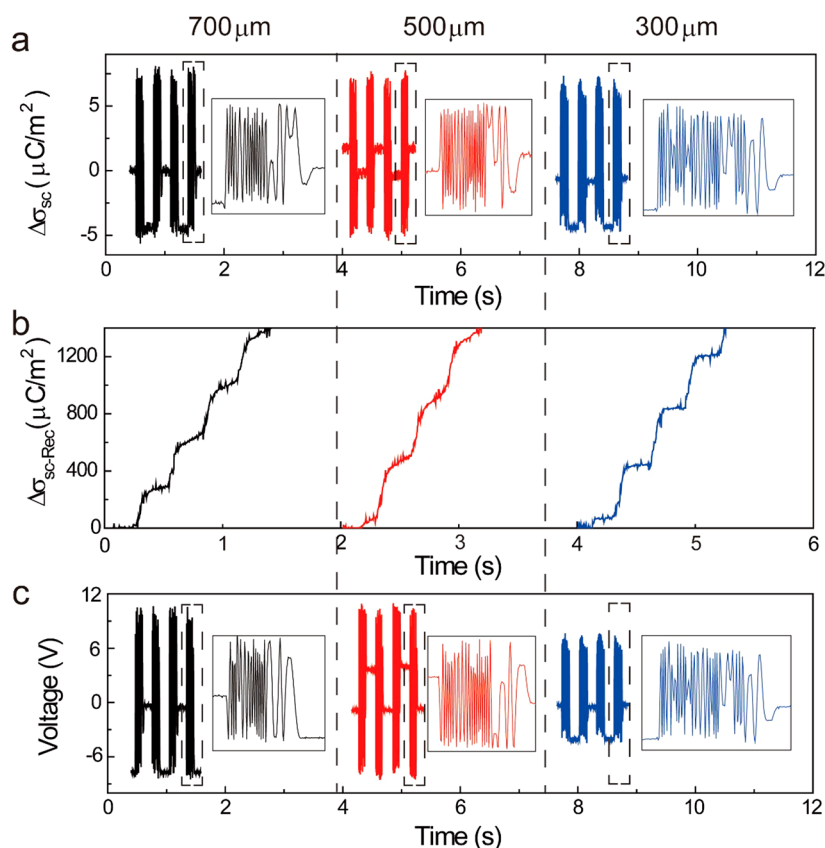
Figure 3. Electrical measurement results of the S-TENG-CGG with different grated structures. (a) The transferred charge ($\Delta\sigma_{SC}$) of the S-TENG-CGG. (b) Accumulated transferred charges ($\Delta\sigma_{SC\text{-}Rec}$). (c) The open-circuit voltage (V_{OC}).

negative charges in steel electrode are transferred into the Cu electrode, and as a result, another electrostatic equilibrium is achieved. This is one unit step of sliding. When the steel mask continues to slide rightward as shown in Figure 1c,iv, the charges are transferred between steel and Cu electrodes with opposite direction, and the current with opposite direction is generated. As the steel electrode continues to move, similar cycles are repeated and an alternating current is generated.

First, it is experimentally verified that the positive charged nylon film becomes negatively charged after the RIE treatment. Two contact-separation mode TENGs are made. The nylon film of the first TENG is treated with RIE and the other TENG is made of a nylon film without RIE treatment for comparison. The transferred charge ($\Delta\sigma_{SC}$) and open circuit voltage of the two TENGs are shown in Figure 2, which shows opposite polarizations. The nylon films with and without RIE treatment have negative and positive triboelectric charges, respectively, which is the reason for their opposite polarizations in transferred charge and open circuit voltage. These results directly demonstrate that the nylon film gains opposite triboelectric potential and triboelectric charges after the RIE process, which is caused by the changing of surface chemical groups during the RIE process.

To experimentally study the influence of the gap width on the output performance, three devices with different gap width (300, 500, and 700 μm) but the same effective area were fabricated, and their electrical characteristics were measured. Figure 3a shows the transferred charge density ($\Delta\sigma_{SC}$) of the S-TENG-CGG and the inset shows the enlarged profiles of a half sliding cycle. A full sliding cycle is composed of two parts with

the left part (not enlarged) corresponding to a one-way sliding and the right one representing the backward process. As can be seen that there are 18, 24, 28 cycles of the tribo-charges transferred for the 700, 500, and 300 μm S-TENG-CGGs, respectively. As the gap decreases from 700 to 300 μm, the maximum $\Delta\sigma_{SC}$ decreases a little (from 12.1 to 11.1 μC/m²). By connecting the S-TENG-CGG with a bridge rectifier, almost all of the transferred charges can be accumulatively collected, for example, in an energy storage device. As shown in Figure 3b, the amount of accumulated charges ($\Delta\sigma_{SC\text{-}Rec}$) is slightly enhanced by the increasing segment numbers because of multiplied charge transfer cycles (from 18 to 28 cycles). According to a previous report, the total transferred charge for a grated structure with N segments is N times as much as that of a flat S-TENG with the same effective area.[37] We think there are two reasons why the $\Delta\sigma_{SC\text{-}Rec}$ values measured in experiments does not linearly increase with segment number: first, the maximum $\Delta\sigma_{SC}$ decreased a little for the device with a larger segment number, so the $\Delta\sigma_{SC\text{-}Rec}$ will be smaller; second, as can be seen, there are many peaks lower than the maximum $\Delta\sigma_{SC}$, as shown in the enlarged part of Figure 3a, which will decrease the $\Delta\sigma_{SC\text{-}Rec}$. The measured open-circuit voltage (V_{OC}) curves are shown in Figure 3c which shows both positive and negative V_{OC} peaks. In the V_{OC} curves of general TENG, there is only either positive or negative V_{OC} peaks, because there is only either positive or negative triboelectric charges in the triboelectric layer. In the previous report about a rotating TENG with a grated structure, there are alternating positive and negative triboelectric charges in the triboelectric layer, where both positive and negative V_{OC} peaks are generated in
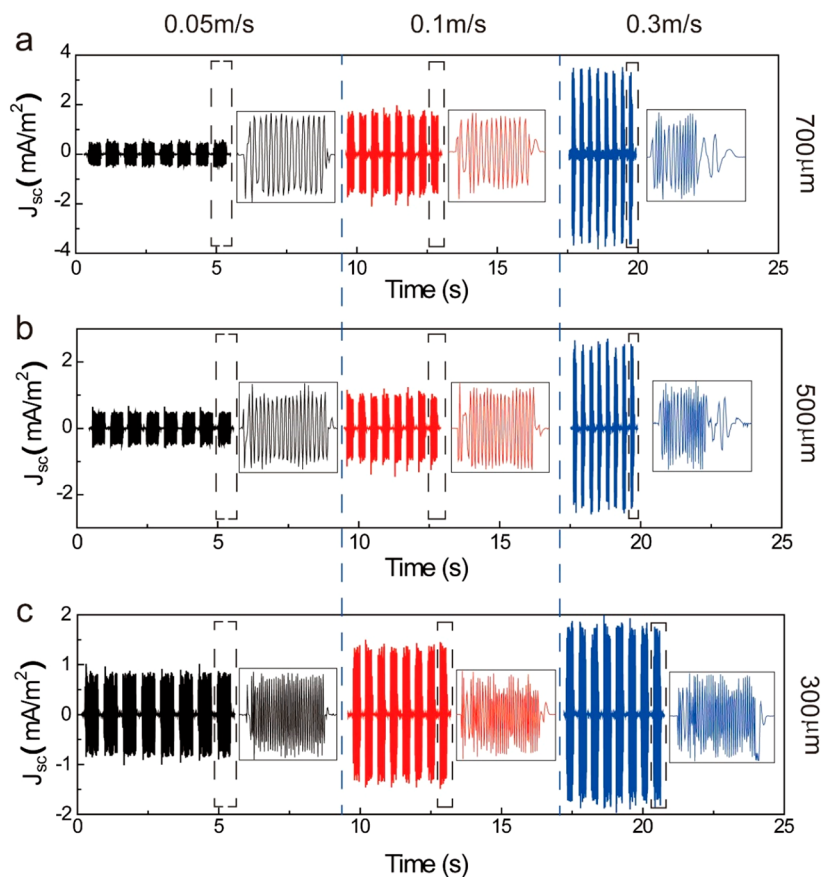
Figure 4. Current densities (J_{SC}) of the S-TENG-CGG with different grated structures at different speeds.
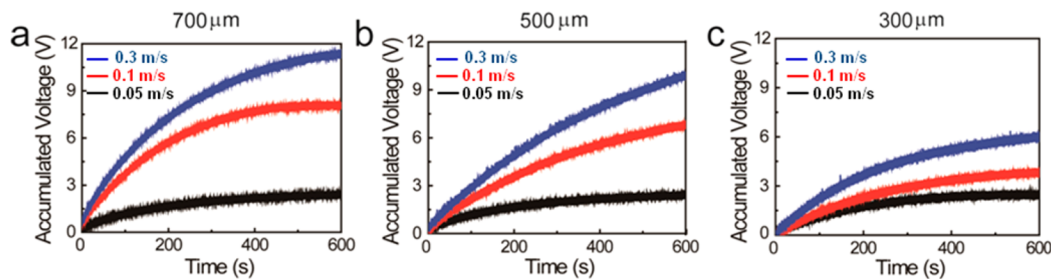

Figure 5. Capacitor charging curves of the S-TENGs under different speeds. (a) S-TENG with 700 μm grated structure. (b) S-TENG with 500 μm grated structure. (c) S-TENG with 300 μm grated structure.

the V_{OC} curves.[9] There is a similar case in our measured V_{OC} curve in Figure 3c, which confirms that the regions with and without RIE etching have opposite triboelectric charges. As shown in Figure 3c, the V_{OC} decreases from about 18.5 to 10.1 V when the gap decreased to 300 μm. It is reported that for the conductor-to-dielectric S-TENG, the V_{OC} is given by[38]

$$V_{OC} = \frac{\sigma x}{\varepsilon_0 (l - x)} \frac{d_2}{\varepsilon_{r2}} \quad (5)$$

where l is the length of the dielectric layer (here is the length of the nylon film), d_2 is the thickness of the dielectric layer (the nylon film), ε_0 and ε_{r2} is the dielectric permittivity of vacuum and the dielectric layer, and x is the lateral separation distance. In our S-TENG-CGG, d_2 is 200 μm. Hence, as the gap (x) decreases from 700 to 300 μm, the V_{OC} decreases much more, as shown in Figure 3c.

As for the current density (J_{SC}), when the sliding movement has a larger speed, the magnitude of J_{SC} increases, as shown in Figure 4. As the moving speed increased from 0.05 to 0.3 m/s, the peak values of J_{SC} increased from 0.78 to 1.76 mA/m^2, 0.45 to 2.32 mA/m^2, and 0.49 to 3.37 mA/m^2 for the 300 μm, 500 μm, and 700 μm gap S-TENG-CGG, respectively. The enhanced performance can be explained by the following equation:[38]

$$J_{SC} = \frac{d\Delta\sigma_{sc}}{dt} \quad (6)$$

where t is the time. Since the length and the time for each unit step will be shorter as the finger number increases, tribo-charges can be transferred faster and hence the higher amplitude and frequency are achieved for the current. Therefore, introducing more fingers in the structure will be
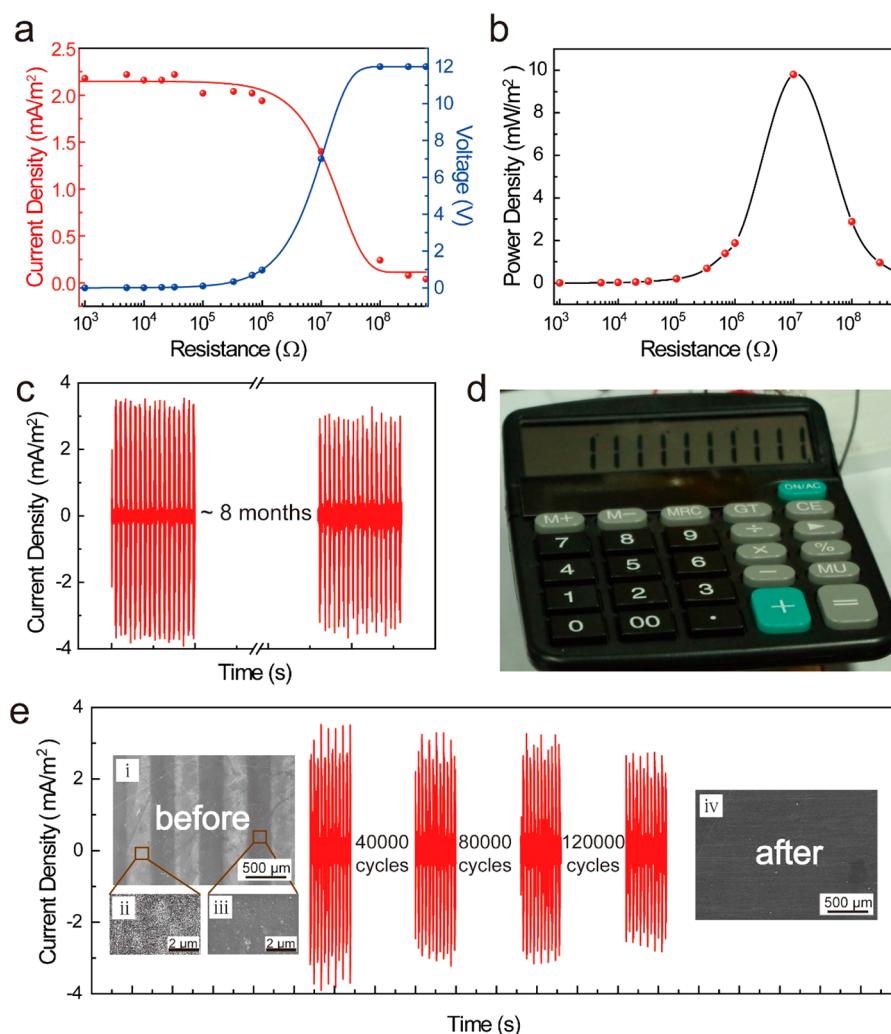
Figure 6. (a) The dependence of the output voltage, current density, and (b) power density on the resistance of the external load. (c) Current density curves of the same S-TENG-CGG measured before and after 8 months. (d) A calculator driven by the S-TENG-CGG. (e) The electrical output curves of S-TENG-CGG during the continuous operation up to 120 000 cycles. Insets are FESEM images of the nylon triboelectric layer before (i) and after (iv) 120 000 operation cycles. Images ii and iii are the enlarged images of the regions with and without RIE treatment, respectively.

favorable for a greater accumulation of charges, larger current density, and higher frequency.

The transferred charges can be accumulatively collected in capacitors. As shown in Figure 5, the accumulated voltages of a 10 μF capacitor are higher when the S-TENG-CGG works at a higher speed no matter the gap of the S-TENG-CGG. However, the accumulated voltage of the capacitor is lower when charged by the S-TENG-CGG with a 300 μm gap than the one with a 700 μm gap at the same speed. This is because the V_{OC} of the S-TENG-CGG with the 300 μm gap is lower than that with the 700 μm gap. Although the S-TENG-CGG with the 300 μm gap can generate more transferred charges, some charges cannot be collected by the capacitor as the increase of the capacitor's voltage, especially when the capacitor's voltage almost reaches the V_{OC} of the S-TENG-CGG.

As a power source in practical use, the S-TENG-CGG will be connected with external loads. Therefore, the actual voltages and current densities on varied load resistances were measured and the results are summarized in Figure 6a. The current density (at the speed of 0.3 m/s) drops at larger external

resistances, while the voltage across the load exhibits a reversed tendency. Accordingly, the power density provided by the S-TENG-CGG first rises at low resistance region and then declines at high resistance, showing a maximum value of 9.8 mW/m^2 at the load resistance of 10 MΩ, as shown in Figure 6b. To experimentally test the stability of the S-TENG-CGG, the current curves of a same device were measured before and after 8 months, the results of which are shown in Figure 6c. This figure shows good stability of the device, which is an effect of the inert and stable chemical groups containing F in the RIE etched nylon film. As shown in Figure 6d, as the output voltage is rectified through a rectifier bridge, the S-TENG-CGG can directly keep up driving a calculator. As shown in Figure 6e, the as-prepared S-TENG-CGG has slight concavo-convex structures due to the reduced height in the RIE treated region, as shown in Figure 6e,i. After 120 000 cycles operation at a speed of 0.3 m/s, the concavo-convex structure completely disappears (Figure 6e,iv) however the output current of the S-TENG-CGG is not significantly reduced. These results clearly indicate that the working principle of the S-TENG-CGG is dependent on the chemical group grated structure, but not dependent on

the concavo-convex structure. After the operation of 120 000 cycles, the weight ratio of F in the nylon surface is reduced from 1.16% to zero in the measured energy dispersive spectrometer, which indicates that the F-group may infiltrate into the nylon film. In the initial stage, the existence of a concavo-convex structure results in greater friction and wear between the nylon film and the stainless steel electrode, which gradually reduces the concavo-convex structure until the nylon film becomes flat and smooth. With the complete disappearance of the concavo-convex structure, the friction and wear are greatly reduced, which makes the S-TENG-CGG maintain a longer working life. Compared with the traditional grated TENGs with mechanical concavo-convex structure reported previously,[21,25] the S-TENG-CGG has a flat and smooth triboelectric layer, which brings advantages in reducing wear and enhancing its working lifetime.

CONCLUSION

Here, we developed a S-TENG with chemical group grated structure based on a triboelectric layer with triboelectric potential positive–negative alternating structure. The triboelectric layer was fabricated through the RIE process with the help of a metal mask with grated structure. After the RIE etching process, the nylon film, originally positively charged as in friction with stainless steel, gained opposite triboelectric potential with a grated structure on its surface because of the change of surface functional groups. The output signals of the S-TENG-CGG are alternating, and the frequency is determined by both the segment numbers and the moving speed. In the S-TENG-CGG, there is no concavo-convex structure, and the frictional resistance and abrasion are largely reduced, which enhances its performances in better stability and longer working life.

EXPERIMENTAL SECTION

Reactive Ion Etching Process. Before the reactive ion etching process, the nylon film was cleaned with deionized water and ethanol. Then the film was deposited a layer of copper (Cu) through magnetron sputtering. Then the film was cut and put under the metal pattern mask. At last, the fluorocarbon plasma treatment of the nylon film surface was conducted using a reactive ion etcher (ME-6A). The RF power, argon flow rate, oxygen flow rate, and carbon tetrafluoride flow rate were set at 200 W, 100 sccm, 80 and 100 sccm, respectively. The chamber pressure was 15 mTorr.

Characterization. For the electric output measurement of the S-TENG, a line motor (LinMot 1100) was applied to drive the S-TENG sliding forward and backward, a programmable electrometer (Keithley model 6514) was used to test the open circuit voltage and transferred charge. A low noise current preamplifier (Stanford Research System modelSR570) was adopted to test the short-circuit current.

AUTHOR INFORMATION

Corresponding Authors
*E-mail: chenggang@henu.edu.cn.
*E-mail: zld@henu.edu.cn.
*E-mail: zhong.wang@mse.gatech.edu.

ORCID
Gang Cheng: 0000-0002-1242-8739
Zhong Lin Wang: 0000-0002-5530-0380

Author Contributions
#W.S. and G.Q.G. contributed equally to this work.

Notes
The authors declare no competing financial interest.

REFERENCES

(1) Fan, F. R.; Tian, Z. Q.; Wang, Z. L. Flexible Triboelectric Generator! *Nano Energy* **2012**, *1*, 328−334.

(2) Grzybowski, B. A.; Winkleman, A.; Wiles, J. A.; Brumer, Y.; Whitesides, G. M. Electrostatic Self-Assembly of Macroscopic Crystals Using Contact Electrification. *Nat. Mater.* **2003**, *2*, 241−245.

(3) Baytekin, H. T.; Patashinski, A. Z.; Branicki, M.; Baytekin, B.; Soh, S.; Grzybowski, B. A. The Mosaic of Surface Charge in Contact Electrification. *Science* **2011**, *333*, 308−312.

(4) Gu, G. Q.; Han, C. B.; Tian, J. J.; Lu, C. X.; He, C.; Jiang, T.; Li, Z.; Wang, Z. L. Antibacterial Composite Film-Based Triboelectric Nanogenerator for Harvesting Walking Energy. *ACS Appl. Mater. Interfaces* **2017**, *9*, 11882−11888.

(5) Hou, T. C.; Yang, Y.; Zhang, H. L.; Chen, J.; Chen, L. J.; Wang, Z. L. Triboelectric Nanogenerator Built Inside Shoe Insole for Harvesting Walking Energy. *Nano Energy* **2013**, *2*, 856−862.

(6) Zhu, G.; Bai, P.; Chen, J.; Wang, Z. L. Power-Generating Shoe Insole Based on Triboelectric Nanogenerators for Self-Powered Consumer Electronics. *Nano Energy* **2013**, *2*, 688−692.

(7) Zheng, Q.; Shi, B. J.; Fan, F. R.; Wang, X. X.; Yan, L.; Yuan, W. W.; Wang, S. H.; Liu, H.; Li, Z.; Wang, Z. L. In Vivo Powering of Pacemaker by Breathing-Driven Implanted Triboelectric Nanogenerator. *Adv. Mater.* **2014**, *26*, 5851−5856.

(8) Zhang, Q.; Liang, Q. J.; Liao, Q. L.; Yi, F.; Zheng, X.; Ma, M. Y.; Gao, F. F.; Zhang, Y. Service Behavior of Multifunctional Triboelectric Nanogenerators. *Adv. Mater.* **2017**, *29*, 1606703.

(9) Guo, H. Y.; Chen, J.; Yeh, M. H.; Fan, X.; Wen, Z.; Li, Z. L.; Hu, C. G.; Wang, Z. L. An Ultrarobust High-Performance Triboelectric Nanogenerator Based on Charge Replenishment. *ACS Nano* **2015**, *0S*, 5577−5584.

(10) Xie, Y. N.; Wang, S. H.; Lin, L.; Jing, Q. S.; Lin, Z. H.; Niu, S. M.; Wu, Z. Y.; Wang, Z. L. Rotary Triboelectric Nanogenerator Based on a Hybridized Mechanism for Harvesting Wind Energy. *ACS Nano* **2013**, *7*, 7119−7125.

(11) Yang, Y.; Zhu, G.; Zhang, H. L.; Chen, J.; Zhong, X. D.; Lin, Z.-H.; Su, Y. J.; Bai, P.; Wen, X. N.; Wang, Z. L. Triboelectric Nanogenerator for Harvesting Wind Energy and as Self-Powered Wind Vector Sensor System. *ACS Nano* **2013**, *7*, 9461−9468.

(12) Wang, S. H.; Mu, X. J.; Wang, X.; Gu, A. Y.; Wang, Z. L.; Yang, Y. Elasto-Aerodynamics-Driven Triboelectric Nanogenerator for Scavenging Air-Flow Energy. *ACS Nano* **2015**, *9*, 9554−9563.

(13) Lin, Z.-H.; Cheng, G.; Wu, W. Z.; Pradel, K. C.; Wang, Z. L. Dual-Mode Triboelectric Nanogenerator for Harvesting Water Energy and as a Self-Powered Ethanol Nanosensor. *ACS Nano* **2014**, *8*, 6440−6448.

(14) Lin, Z.-H.; Cheng, G.; Lee, S. M.; Pradel, K. C.; Wang, Z. L. Harvesting Water Drop Energy by a Sequential Contact-Electrification and Electrostatic-Induction Process. *Adv. Mater.* **2014**, *26*, 4690−4696.

(15) Cheng, G.; Lin, Z.-H.; Du, Z. L.; Wang, Z. L. Simultaneously Harvesting Electrostatic and Mechanical Energies from Flowing Water by a Hybridized Triboelectric Nanogenerator. *ACS Nano* **2014**, *8*, 1932−1939.

(16) Lin, Z.-H.; Cheng, G.; Lin, L.; Lee, S. M.; Wang, Z. L. Water-Solid Surface Contact Electrification and Its Use for Harvesting Liquid Wave Energy. *Angew. Chem., Int. Ed.* **2013**, *5*, 12545−12549.

(17) Wang, Z. L. New Wave Power. *Nature* **2017**, *542*, 159−160.

(18) Wang, Z. L. Triboelectric Nanogenerators as New Energy Technology for Self-Powered Systems and as Active Mechanical and Chemical Sensors. *ACS Nano* **2013**, *7*, 9533−9557.

(19) Ahmed, A.; Hassan, I.; Ibn-Mohammed, T.; Mostafa, H.; Reaney, I. M.; Koh, L. S. C.; Zu, J.; Wang, Z. L. Environmental Life Cycle Assessment and Techno-Economic Analysis of Triboelectric Nanogenerators. *Energy Environ. Sci.* **2017**, *10*, 653−671.

(20) Wei, X. Y.; Zhu, G.; Wang, Z. L. Surface-Charge Engineering for High-Performance Triboelectric Nanogenerator Based on Identical Electrification Materials. *Nano Energy* **2014**, *10*, 83−89.

(21) Zhou, Y. S.; Zhu, G.; Niu, S. M.; Liu, Y.; Bai, P. S.; Jing, Q.; Wang, Z. L. Nanometer Resolution Self-Powered Static and Dynamic Motion Sensor Based on Micro-Grated Triboelectrification. *Adv. Mater.* **2014**, *26*, 1719−1724.

(22) Yang, Y.; Zhou, Y. S.; Zhang, H. L.; Liu, Y.; Lee, S. M.; Wang, Z. L. A Single-Electrode Based Triboelectric Nanogenerator as Self-Powered Tracking System. *Adv. Mater.* **2013**, *25*, 6594−6601.

(23) Wang, S. H.; Xie, Y. N.; Niu, S. M.; Lin, L.; Wang, Z. L. Freestanding Triboelectric-Layer-Based Nanogenerators for Harvesting Energy from a Moving Object or Human Motion in Contact and Non-Contact Modes. *Adv. Mater.* **2014**, *26*, 2818−2824.

(24) Chen, X. Y.; Jiang, T.; Wang, Z. L. Modeling a Dielectric Elastomer as Driven by Triboelectric Nanogenerator. *Appl. Phys. Lett.* **2017**, *110*, 033505.

(25) Xie, Y. N.; Wang, S. H.; Niu, S. M.; Lin, L.; Jing, Q. S.; Yang, J.; Wu, Z. Y.; Wang, Z. L. Grated-Structured Freestanding Triboelectric-Layer Nanogenerator for Harvesting Mechanical Energy at 85% Total Conversion Efficiency. *Adv. Mater.* **2014**, *26*, 6599−6607.

(26) Yang, Y.; Zhu, B. P.; Yin, D.; Wei, J. H.; Wang, Z. Y.; Xiong, R.; Shi, J.; Liu, Z. Y.; Lei, Q. Q. Flexible Self-Healing Nanocomposites for Recoverable Motion Sensor. *Nano Energy* **2015**, *17*, 1−9.

(27) Jing, Q. S.; Xie, Y. N.; Zhu, G.; Han, R. P. S.; Wang, Z. L. Self-Powered Thin-Film Motion Vector Sensor. *Nat. Commun.* **2015**, *6*, 8031.

(28) Li, X. H.; Han, C. B.; Jiang, T.; Zhang, C.; Wang, Z. L. A Ball-Bearing Structured Triboelectric Nanogenerator for Nondestructive Damage and Rotating Speed Measurement. *Nanotechnology* **2016**, *27*, 085401.

(29) Xiang, C. H.; Liu, C. R.; Hao, C. L.; Wang, Z. K.; Che, L. F.; Zhou, X. F. A Self-Powered Acceleration Sensor with Flexible Materials based on Triboelectric Effect. *Nano Energy* **2017**, *31*, 469−477.

(30) Diaz, A. F.; Felix-Navarro, R. M. A Semi-Quantitative Tribo-Electric Series for Polymeric Materials: the Influence of Chemical Structure and Properties. *J. Electrost.* **2004**, *62*, 277−290.

(31) Li, H. Y.; Su, L.; Kuang, S. Y.; Pan, C. F.; Zhu, G.; Wang, Z. L. Significant Enhancement of Triboelectric Charge Density by Fluorinated Surface Modification in Nanoscale for Converting Mechanical Energy. *Adv. Funct. Mater.* **2015**, *25*, 5691−5697.

(32) Raoux, S.; Tanaka, T.; Bhan, M.; Ponnekanti, H.; Seamons, M.; Deacon, T.; Xia, L. Q.; Pham, F.; Silvetti, D.; Cheung, D.; Fairbairn, K.; Jonhson, A.; Pearce, R.; Langan, J. Remote Microwave Plasma Source for Cleaning Chemical Vapor Deposition Chambers: Technology for Reducing Global Warming Gas Emissions. *J. Vac. Sci. Technol., B: Microelectron. Process. Phenom.* **1999**, *17*, 477−485.

(33) Scott, P. M.; Matienzo, L. J.; Babu, S. V. Cf_4/O_2 Plasma-Etching and Surface Modification of Polyimide Films - Time-Dependent Surface Fluorination and Fluorination Model. *J. Vac. Sci. Technol., A* **1990**, *8*, 2382−2387.

(34) Zhang, L.; Chin, W. S.; Huang, W.; Wang, J. Q. Investigation of the Surface Structures and Dynamics of Polyethylene Terephthalate (PET) Modified by Fluorocarbon Plasmas. *Surf. Interface Anal.* **1999**, *28*, 16−19.

(35) Iriyama, Y.; Yasuda, T.; Cho, D. L.; Yasuda, H. Plasma Surface Treatment on Nylon Fabrics by Fluorocarbon Compounds. *J. Appl. Polym. Sci.* **1990**, *39*, 249−264.

(36) Wei, X.; Xiaodong, C.; Jianqi, W. Characterization of PET Surface Modification with CF_4-CH_4 (CF_4/CH_4-Greater-Than-5) RF Plasma by XPS and Contact-Angle Techniques. *J. Polym. Sci., Part A: Polym. Chem.* **1995**, *33*, 807−813.

(37) Yi, F.; Lin, L.; Niu, S. M.; Yang, P. K.; Wang, Z. N.; Chen, J.; Zhou, Y. S.; Zi, Y. L.; Wang, J.; Liao, Q. L.; Zhang, Y.; Wang, Z. L. Stretchable-Rubber-Based Triboelectric Nanogenerator and Its Application as Self-Powered Body Motion Sensors. *Adv. Funct. Mater.* **2015**, *25*, 3688−3696.

(38) Niu, S. M.; Liu, Y.; Wang, S. H.; Lin, L.; Zhou, Y. S.; Hu, Y. F.; Wang, Z. L. Theory of Sliding-Mode Triboelectric Nanogenerators. *Adv. Mater.* **2013**, *25*, 6184−6193.